Spatial, Temporal, and Thermal Analysis of a Cavitating High-Pressure Water-Jet

C. A. Fairfield

School of Engineering & Information Technology, Charles Darwin University, Australia.
charlie.fairfield@cdu.edu.au

Abstract-*A cavitating high-pressure water-jet (as used for testing the erosion resistance of pipelines) was examined using high-speed photography, thermography, and image analysis to describe the relationships between spatial and temporal fluctuations observed in the flow and the temperature fields at pressures reaching 69 MPa. Frictional heating of the jet, as it left the nozzle, increased as the pressure increased. The increase from 13.8 MPa to 69.0 MPa was 2.9 K (70.7%) on the minimum, and 2.6 K (29.9%) on the maximum, temperatures measured. Good correlation was seen between the upper and lower jet-edge frequencies which ranged from 4.5 Hz to 6.8 Hz. Correlation coefficients were 0.85 and 0.97 respectively. The jet's lower edge was influenced by temperature at lower x/d_n values ($x/d_n \leq 2$), with correlation coefficients at $x/d_n = 1$ and 2 of 0.80 and 0.87, respectively. This experimental characterisation of a high-pressure water-jet is offered as a baseline case suitable for benchmarking against any of the packages (or models developed on an ad hoc basis) used for the numerical analysis and simulation of multiphase fluid flows.* **Copyright © 2016 Penerbit Akademia Baru - All rights reserved**

Keywords – High-pressure water-jet, Cavitation, Thermography, Image analysis.

1.0 INTRODUCTION

The objective of the work was the investigation of the occurrence of cavitation in a high-pressure water-jet and how it was influenced by both external and system-induced effects. To that end, the UK industry standard jetting nozzle from the Water Research Centre (WRc) was used at a range of pressures and the flow captured with a view to measuring the spatial, temporal, and thermal variations therein. The output data were presented as an experimental benchmark against which future numerical analysis/computational fluid dynamics derived numerical solutions maybe assessed. The research fills gaps in current knowledge insofar as it relates to spray patterns of use to agricultural technologists as they seek to minimise water use while achieving uniformity of water distribution in nozzle irrigation systems [1]. Recent research into improving rice yield may also benefit from a better template upon which to base the design of spray-based fertiliser and seed distribution systems [2]. Fuel injection systems also rely heavily on the ability of the engineer to control the profile and break-up of jets containing multi-phase fluid flows (*e.g.* kerosene and air [3]): this research also provides experimental verification of the break-down of the coherence of the jet into droplets (spray), the mechanics of which have been studied elsewhere using computational fluid dynamics [4].

2.0 EXPERIMENTAL WORK

Figures 1 and 2 show the test set-up: a WRc jetting test ensemble to Water Industry Standard (WIS) 4-35-01 was used [5]. This comprised a pipe constriction (12.7 mm down to a nozzle diameter d_n of 1.5 mm in a series of step-jumps over a length of 62 mm), that accelerated the energised fluid flow to atmosphere to yield the required pressure drop to induce cavitation in the resulting high-pressure water-jet.
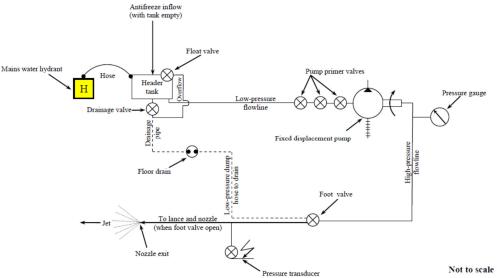

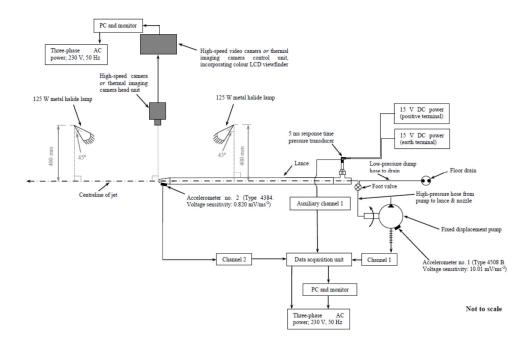
Figure 1: General arrangement of the hydraulic equipment

Figure 2: Instrumentation layout

2

Figure 3 shows a cross-section through the nozzle. A 91 kW, six-cylinder, 5.8 litre, positive-displacement, plunger pump was used to deliver the required water pressures and flow rates. Figure 4 shows both pump and system characteristics and its efficiency η_p. It was fed with mains water by stand-pipe and 63.5 mm internal diameter hose. The energised water was fed to the nozzle through a 12.7 mm internal diameter high-pressure line. A steel mounting block was welded to the top side of the safety cage. The lance was set at an angle $\alpha = 30°$ to the horizontal and at a vertical stand-off height of 5 mm, as measured from a horizontal reference plane (see Figure 5).
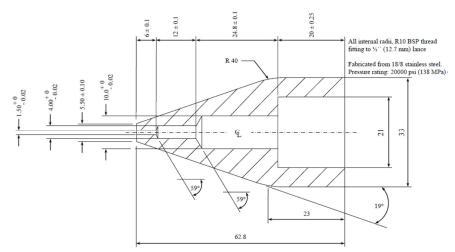

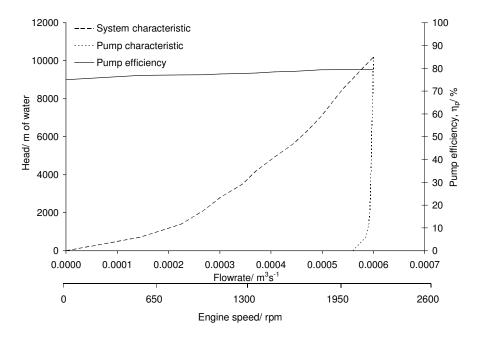**Figure 3**: Longitudinal cross-section through the nozzle (all dimensions mm)

Figure 4: Pump and system characteristics: head and pump efficiency *versus* volumetric flow and engine speed
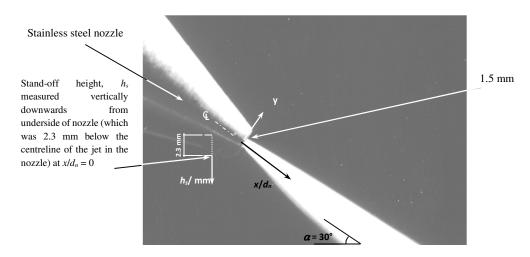
Figure 5: The nozzle and jet running in free air

2.1 Pressure Measurement

A Gems 1000 series, 100 MPa range, pressure transducer with a 1 ms response time was installed in series with the lance: its output was logged by a Brüel & Kjær PULSE spectrum analyser system, to give continuous logging of pressure and time. The output voltage range, corresponding to the aforementioned pressure range was 0 V to 5 V which gave an output of 5 mV *per* 0.1 MPa, with an accuracy of 0.25% of full scale deflection (12.5 mV $\equiv$ 0.25 MPa). The 12.7 mm diameter stainless steel lance, with a digital pressure gauge was fixed to the mounting block and the apparatus levelled to $\pm\,0.05°$ in both lateral and longitudinal directions.

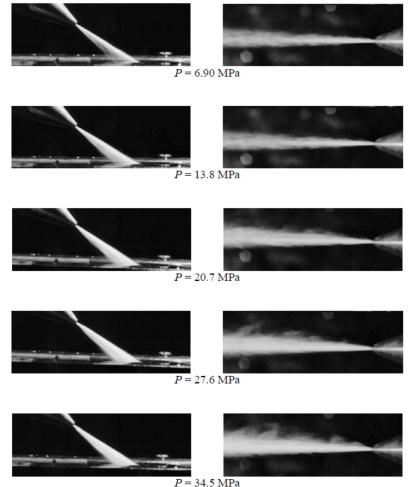### 2.2 Optical Measurement: High-resolution Still Photographs

Figure 6 shows still photographs of the jet at $\alpha = 30°$ taken horizontally and vertically at pressures ranging from 6.90 MPa to 34.5 MPa in 6.90 MPa increments. Figure 6 shows three zones in the jet: an upper spray zone, the core, and the lower spray zone. The spray zones were asymmetrical. Tollmien-Schlichting structures [6, 7] were visible especially in the vertical photographs at pressure $P \geq 20.7$ MPa.

2.3 Optical Measurement: CCD Camera Footage

The contact footprint of the jet was imaged as it impinged upon a surface, this lead to a better understanding of the jet cross-section (in particular its footprint shape and contact area). A charge-coupled device (CCD) camera (YD 66, 12 V (direct current), 2.3 megapixel, black/white image, 0.02 lux, Vivitek Inc., Taiwan) was attached to the rig. The CCD camera was mounted beneath a sheet of transparent polymethylmethacrylate (PMMA) which allowed the camera to record footage of the jet as it impinged on the PMMA sheet. PMMA has a relatively poor jetting resistance, the jetting pressure was restricted to one which, from experience [8-10], would not cause penetration and damage the camera: *i.e.* 27.6 MPa for two minutes, with $h_s = 5$ mm and $\alpha = 30°$. Real-time footage from the CCD camera was recorded directly to a computer: stills from this footage are shown in Figure 7.
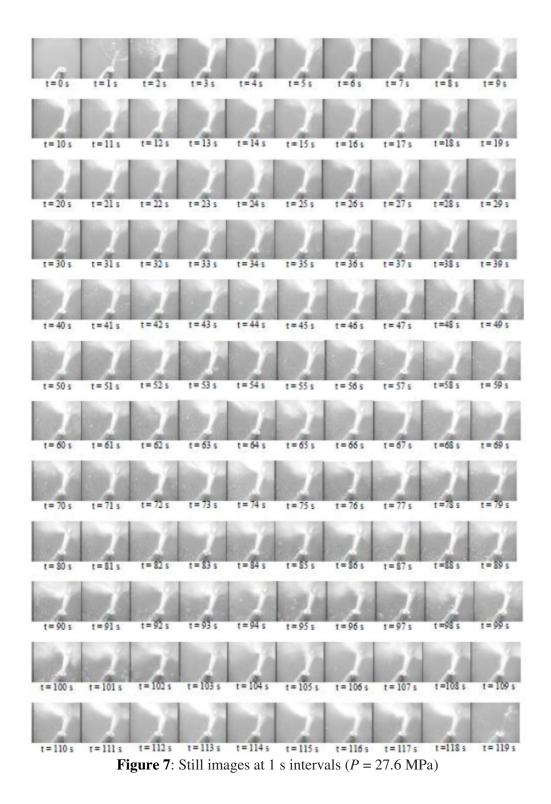
$P = 6.90$ MPa

$P = 13.8$ MPa

$P = 20.7$ MPa

$P = 27.6$ MPa

$P = 34.5$ MPa

Figure 6: Horizontal and vertical still photographs of the jet

Positioning the camera beneath translucent PMMA, as it was being jetted, made it possible to see how the jet dispersed. Figure 7 shows still images taken from the CCD footage at 1 s intervals. These images served to show global fluctuations in the size and shape of the jet over a longer duration than the high-speed video (see Section 2.4). An idealised geometrical representation of the jet (Figures 8 and 9) and its impact zone on the imaginary plane of reference were generated to complement the CCD footage and still photographs.

2.4 Optical Measurement: High-speed Video Footage

This set of experiments was central to gaining an insight into the jet geometry (its spatial and temporal fluctuations) and to characterise the jet. Visible evidence of bubbles and their fluctuations in the flow was sought. The composition of the jet, in terms of its constituent parts (upper spray zone, lower spray zone, and core) was also investigated with a view to relating these facets to other jet/jetting system behaviours. As the jet was travelling at high nozzle exit velocities v_j, high-speed video capture was used to aid jet characterisation. The exit velocities (and Mach number equivalents) are shown in Table 1: the distances travelled by the jet in a 50 μs frame interval, and a 10 μs lens shutter interval, were also calculated.
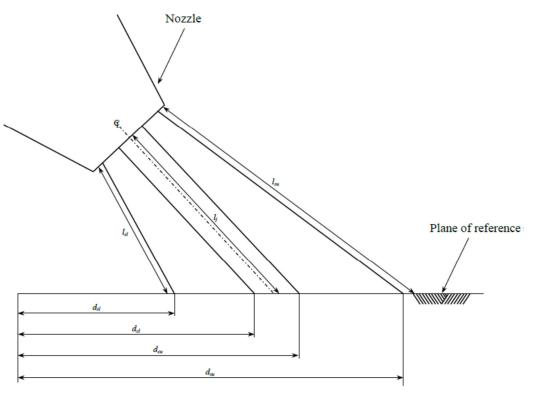
Figure 7: Still images at 1 s intervals (P = 27.6 MPa)

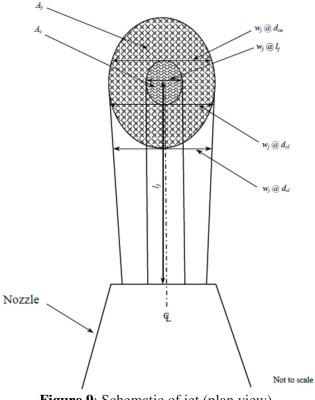**Figure 8**: Schematic of jet (horizontal elevation)

Figure 9: Schematic of jet (plan view)

Table 1: Exit velocities for the range of pressures used

Pressure/ MPa	v_j/ ms^{-1}	Ma/ numeric	Frame: distance travelled in 50 µs/ mm
			Shutter: distance travelled in 10 µs/ mm
13.8	166.1	0.49	8.31
			1.66
27.6	234.9	0.70	11.8
			2.35
41.4	287.7	0.85	14.4
			2.88
55.2	332.2	0.99	16.6
			3.32
69.0	371.4	1.10	18.6
			3.71
82.8	406.9	1.21	20.4
			4.07

By using a 20,000 frames *per* second recording rate and the 10 µs shutter speed setting on an RX-6 Memrecam (NAC Systems, Simi Valley, Ca, USA) and two 125 W metal halide lamps to illuminate the jet, footage was recorded and stored electronically (Figure 2). The purpose of these tests was to build upon the work of Kobayashi *et al*. [11] and characterise the jet in terms of the frequency of the periodic and ergodic temporal and spatial fluctuations of the cavities along the jet length due to bubble clouds. A study of the self-excited oscillation of the jet and the unsteady cavity discharge caused by the explosive growth of bubble clouds and vortex ring cavitation was carried out by capturing stills from the footage recorded and using image analysis techniques such as thresholding and edge detection. Edge detection techniques [12] were used to differentiate between the zones of the jet and measure them at different positions along its length. This enabled analysis of the doubling length of the jet (*i.e.* the length where the jet width = $2d_n$ which was an indication of the coherence of the jet, which is in turn an indication of the size of the contact area of the jet on any surface upon which it was incident). The jet was captured running free in air, at a range of pressures, with α kept constant at 30°.

Imaging the jet at 20,000 frames *per* second helped to develop an understanding of its behaviour. The composition of the jet (upper and lower spray zones, and core) was also investigated in terms of the spatial and temporal fluctuations in the jet and analysed in conjunction with these data. Figure 10 shows still images from the high-speed video footage, at a range of pressures: the spatial fluctuations in the jet can be seen. Still images decompiled from the high-speed video footage were processed in Adobe Photoshop© using thresholding techniques to isolate the jet from any background perturbations such that only the jet was imaged (Figures 11 and 12). Figure 11 compares different thresholding levels applied to the original stills of Figure 10; the intermediate thresholding value of 32 was used, as this gave the most accurate replication of the edge of the jet. This involved creating a batch file and processing each individual still image. Further processing required that the images be rotated to the horizontal to obtain optimum results: coordinates were then extracted from the threshold-processed images and plotted for analysis.
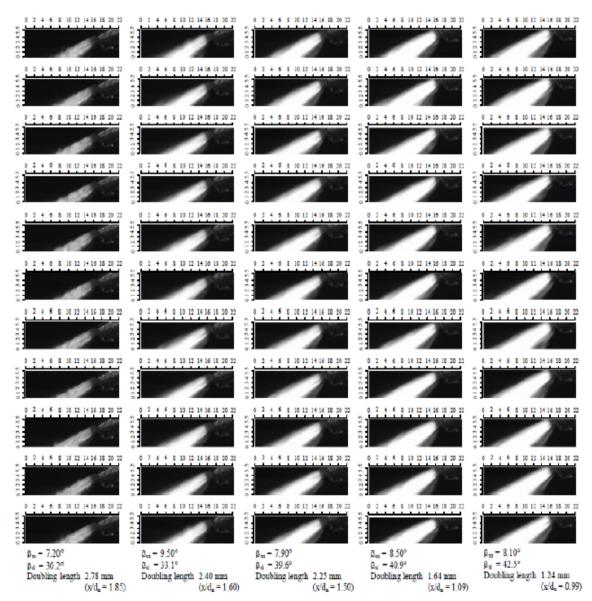
Figure 10: Still images at 50 μs intervals from high-speed video footage (scale in mm)

To quantify the flow rate, integration of the solid of revolution formed by the chosen jet profile over distance $(b - a)$ was undertaken in accordance with (1):

$$V = \int_a^b y^2 \mathrm{d}x \tag{1}$$

The jet was asymmetrical, so an average of the upper and lower edges detected by the "Med (32 used)" thresholding techniques was used (x/d_n and y/d_n with $d_n = 1.5$ mm), resulting in a smooth transition between upper and lower spray zones. The linear best fit is given by (2):

$$y = 0.2037x + 0.75 \tag{2}$$

This gave a flow rate of 0.001595 m^3s^{-1} which was greater than that measured by ultrasonic flow meter (0.000225 m^3s^{-1}) because the spray was included in the thresholding. If the core of the jet were assumed to be cylindrical, then its volume over a 9 mm length was 15.9 mm^3, giving a flow rate of 0.000293 m^3s^{-1}, which was approximately equal to that measured by ultrasonic flow meter. The discrepancy could therefore be attributed to spray.

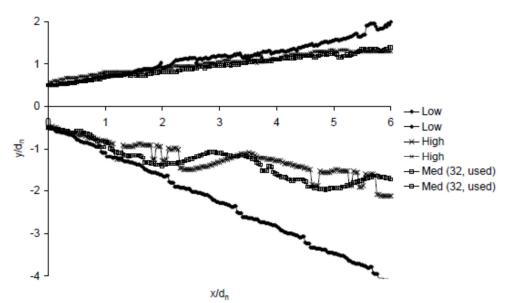**Figure 11**: Thresholding process applied to still images in Figure 10

Figure 12: Typical (P = 13.8 MPa) comparison of low, medium, and high thresholding levels.

3.0 ANALYSIS OF THE GEOMETRICAL PROPERTIES OF THE JET

As mentioned in Section 2.3, an idealised jet geometry was used for application to the various methods of imaging used. This idealisation was based upon a jet with a core that stays parallel and spray-zones that dissipated at a given angle. Figures 8 and 9 show this schematic idealisation in the vertical and horizontal planes (dimensions are as listed in Tables 2 and 3).

Table 2: Definitions: idealised jet geometry (elevation)

Measurement (elevation)	Description
l_j	Length of the centreline of the jet from the nozzle exit to the plane of reference
d_{sl}	Distance from the nozzle exit to the edge of the lower spray zone
d_{su}	Distance from the nozzle exit to the edge of the upper spray zone
d_{cl}	Distance from the nozzle exit to the lower edge of the jet core
d_{cu}	Distance from the nozzle exit to the upper edge of the jet core
l_c	Length of the core of the jet
l_{sl}	Length of the lower spray zone
l_{su}	Length of the upper spray zone
TWL	Total wetted length

Table 3: Definitions: idealised jet geometry (plan)

Measurement (plan)	Description
W_j @ d_{sl}	Width of the jet at the lower spray zone edge
W_j @ d_{su}	Width of the jet at the upper spray zone edge
W_j @ d_{cl}	Width of the jet at the lower edge of the jet core
W_j @ d_{cu}	Width of the jet at the upper edge of the jet core
W_j @ d_{lj}	Width of the jet where the centre line of the core cuts the plane of reference
A_j	Total footprint area of the jet
A_c	Footprint area of the jet core

In Figures 8 and 9 the spray dissipated in both the horizontal and the vertical planes. Tables 4 and 5 show the measured spray angles of the jet, in both the horizontal (upper and lower) and vertical (left and right) planes, as measured from the still images and high-speed video camera, respectively. The only vertical images are from the still camera, hence only these provided measureable left and right spray angles.

Table 4: Measured spray angles (still images)

P/ MPa	Spray angle lower β_{sl}/ °	Spray angle upper β_{su}/ °	Spray angle left β_l/ °	Spray angle right β_r/ °	Doubling length (including spray)/ mm
6.90	25.0	8.00	4.03	4.03	3.02
13.8	34.0	9.50	4.08	4.08	2.80
20.7	39.5	8.50	4.09	4.09	2.62
27.6	37.5	10.5	4.05	4.05	2.49
34.5	36.5	6.50	4.00	4.00	2.34

Table 5: Measured spray angles (high-speed video camera)

P/ MPa	Spray angle lower β_{sl}/ °	Spray angle upper β_{su}/ °	Doubling length (including spray)/ mm
13.8	30.2	7.20	2.78
27.6	33.1	9.50	2.40
41.4	39.6	7.90	2.25
55.2	40.9	8.50	1.64
69.0	42.5	8.10	1.28

The jet trajectory was investigated as it exited the nozzle to ascertain whether or not there was any discernible difference for each pressure. There was not: each pressure showed identical trajectories which were ostensibly linear and emanated from the nozzle exit.

As mentioned, fluctuations in the size and shape of the jet were evident, although the frequencies that can be extracted were limited by the frame rate of the camera (30 frames *per* second, *c.f.* 20,000 frames *per* second for the high-speed video camera). In general, fluctuations in the jet size and shape were seen at a frequency of 1.13 Hz; the vorticity of the flow was also evident from the CCD camera stills; the rotational frequency of the vortices was observed to be approximately 2 Hz to 3 Hz.

Table 6: Frequencies of jet edge fluctuation

P/ MPa	$x/d_n = 1$		$x/d_n = 2$		$x/d_n = 3$	
	f_0 lower/ kHz	f_0 upper/ kHz	f_0 lower/ kHz	f_0 upper/ kHz	f_0 lower/ kHz	f_0 upper/ kHz
13.8	6.2	4.7	6.1	5.6	5.8	5.6
27.6	6.1	4.5	5.6	5.2	5.7	5.1
41.4	6.3	5.5	6.5	5.4	6.2	6.1
55.5	6.8	6.5	6.1	5.9	6.2	5.9
69.0	6.5	5.7	6.2	5.9	6.5	5.8
P/ MPa	$x/d_n = 4$		$x/d_n = 5$		$x/d_n = 6$	
	f_0 lower/ kHz	f_0 upper/ kHz	f_0 lower/ kHz	f_0 upper/ kHz	f_0 lower/ kHz	f_0 upper/ kHz
13.8	6.1	5.1	5.9	5.1	5.4	5.1
27.6	6.3	6.0	5.9	5.2	5.2	4.6
41.4	6.3	5.9	6.4	5.9	6.7	5.9
55.5	6.2	6.0	6.3	6.1	6.7	6.4
69.0	6.3	6.1	6.6	6.0	6.1	5.9

The high-speed video footage gave the data in Table 6 (taken from fluctuations in the upper and lower edges of the jet for $1 \leq x/d_n \leq 6$ over 13.8 MPa $\leq P \leq$ 69.0 MPa). The lower edge of the jet fluctuated over a smaller range as x/d_n increased, whereas the converse was true for the upper edge. The behaviour of the upper edge was indicative of the jet beginning to break-up into the Tollmien-Schlichting structures mentioned previously, due to friction at the air/water interface.

The behaviour of the bottom edge (fluctuating over a smaller range as x/d_n increased) was indicative of the jet stabilising: because the lower spray zone was larger than the upper spray zone, it would have been less susceptible to degeneration into the Tollmien-Schlichting structures seen along the upper edge of the jet.

The variation in jet width increased as x/d_n increased: the jet was divergent. At higher pressures these fluctuations became larger as the Reynolds number increased and the jet became more turbulent (indeed, the jet fluctuated over a greater range at 69.0 MPa, for all x/d_n values, than it did at 13.8 MPa).

4.0 THERMAL MEASUREMENT: THERMOGRAPHY

Cavitation emits sound [13], light [14], and heat [15] under certain circumstances. Therefore, it was decided to record the jet, running in air, with a thermal imaging camera, at a range of pressures, to measure the temperature distribution therein. The temperatures measured were not just attributable to cavitation; because the jet was travelling at velocities sometimes exceeding Ma = 1 the water was frictionally heated along the high-pressure line, and especially at the nozzle.

A camera (an AGEMA (now FLIR) Thermovision® 470 with: an accuracy of ± 2 % of the Celsius temperature T, a range of 20 °C ≤ T ≤ 500 °C, and a sensitivity of ± 0.1 °C at 30 °C) was calibrated by imaging a thin matt black plate (with a constant emissivity of 0.98) at a uniform temperature; 15 thermocouple temperature measurements were taken, covering the surface of the plate. The nozzle was also painted black so that when the jet flowed, it acted as a contrasting object in the camera's field of view to allow the level and sensitivity to be set to approximately mid-range. The level control set the temperature range to be measured, and the sensitivity fine-tuned within that range. The detector was a Mullard SPRITE (HgCdTe) short wave (2 µm ≤ λ_T ≤ 5 µm) type sensor using Peltier cooling and operating at a line frequency of 4 kHz. The resultant spatial resolution was 100 elements *per* line over a field of view of 12° × 12° at 0.65 m from the jet. The jet was run over 13.8 MPa ≤ P ≤ 69.0 MPa for 120 s, and the footage recorded on Hi8™ tape for export to a personal computer with a data capture card; subsequent analysis investigated the global temperature change between pressures and also the temperature change as a function of time for a given pressure.

4.1 Thermography and Temperature Measurement

This section describes data obtained from thermal image camera footage of the divergent jet over 13.8 MPa ≤ P ≤ 69.0 MPa. This revealed the temperature changes in the jet, initially to ascertain whether or not energy changes could be accounted for by hydrodynamics alone, or were indicative of cavitation occurring as the heat transfer was not fully explained by a combination of frictional and adiabatic changes. Not only this, but as the jetting pressure increased, the exit velocity of the jet increased hence the thermal imaging camera also detected frictional heating in the jet: this was evident at the nozzle as d_n decreased from 12.7 mm to 1.5 mm, thus accelerating the flow. Also evident was frictional heating along the edge of the jet at the air-water interface. Different techniques were used to extract key data from raw colour plot thermal images (Figure 13) which showed that temperature increased with jetting pressure.
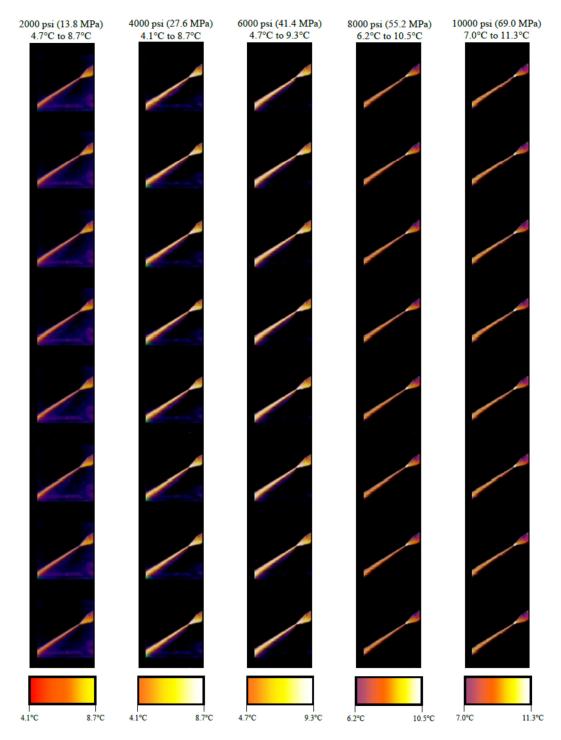
Figure 13: Still images extracted from thermal imaging camera footage

The increase from 13.8 MPa to 69.0 MPa was 2.9 K (70.7%) on the minimum, and 2.6 K (29.9%) on the maximum, temperatures measured. This was due to the aforementioned effects of frictional heating both at the nozzle and at the air-water interface once the jet emerged to atmosphere. In-house software [12] enabled further processing of the raw data so that more meaningful results could be derived (see Figure 14, in which still images from the thermal

imaging camera footage (all for $x/d_n = 3$) may be seen). Each plot (from left to right and top to bottom) represents a 0.033 s time increment from the previous plot).

Figure 14: Typical graphical output from the software [12]
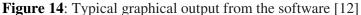
Table 7 shows the derived frequencies of temperature fluctuation in the jet.

Table 7: Frequency of temperature fluctuations in the jet

P/ MPa	$x/d_n = 1$ f_0/ Hz	$x/d_n = 2$ f_0/ Hz	$x/d_n = 3$ f_0/ Hz	$x/d_n = 4$ f_0/ Hz	$x/d_n = 5$ f_0/ Hz	$x/d_n = 6$ f_0/ Hz
13.8	7.2	6.8	7.4	7.6	8.1	7.2
27.6	6.6	6.2	7.6	7.8	7.0	8.2
41.4	8.0	7.2	7.6	8.0	7.6	7.0
55.5	7.8	8.8	8.0	7.8	8.2	8.0
69.0	7.8	8.0	7.6	7.8	7.0	7.8

Figure 15 shows the correlation between the upper and lower jet edge fluctuation frequencies: correlation between the two frequencies was expected as jet edge fluctuations were governed by vibration induced by the hydrodynamic action of the pump. With regards the lack of correlation (Figure 16) between the frequencies of the jet edge, and temperature, fluctuations (the exception being the lower jet edge at $x/d_n = 1$ and $x/d_n = 2$) it was suggested that the fluctuation of the lower edge was temperature driven, given that the highest temperatures (Figure 13) were found at the nozzle exit ($x/d_n = 0$). There was good correlation only at low x/d_n values ($x/d_n = 1$), for nozzle fluctuation frequency and both edge fluctuations suggesting that the dynamic response of the nozzle only influenced the jet up to $x/d_n = 1$: thereafter, the jet was free from the effects of pump vibrations and any fluctuations were governed by perturbations at the air-water interface. The temperature fluctuations and the dynamic response of the jetting system were well correlated at $x/d_n \leq 3$. Vortex ring cavitation frequencies (in the kHz range, Kobayashi $et~al.$ [11]) were not found. Cavitating bubble oscillation frequencies (modelled by the Rayleigh-Plesset equation [15]) were not correlated to the dynamic response of the pump and nozzle, but good correlation ($0.75 \leq r^2 \leq 0.85$) with the jet edge fluctuations, and a similar relationship with the temperature fluctuations ($r^2 = 0.8$ at $x/d_n = 2$). Analysis of the dominant cavitating bubble size's fundamental frequency [8, 12] and its growth-collapse-regrowth cycle is beyond the scope of this paper.
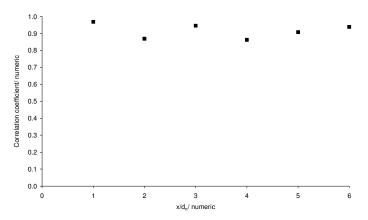

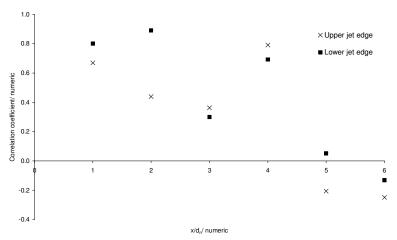**Figure 15**: Correlation of upper and lower jet edge fluctuation frequencies

Figure 16: Correlation of upper and lower jet edge fluctuation frequencies with the frequencies of the measured temperature fluctuations

5.0 CONCLUSIONS

Still photography, CCD camera, and high-speed video imaging were used to characterise the behaviour of a cavitating high-pressure water-jet. This work served to analyse the spatial and temporal fluctuations in the jet, obtain doubling lengths, spray/core identification, spray angles, idealised geometry, flow rate corroboration, and real-time development of the flow regime. Thermal imaging techniques were used to ascertain the temperature regime in the jet at a range of pressures: temperature fluctuations in the jet were also measured.

Spectral analysis gave time- and frequency-domain information about the system for a range of cases. Measurements were taken at both pump and nozzle: the effects were related to other phenomena prevalent in the jet, with specific reference to their dominant frequencies.

The frictional heating of the jet as it exited the nozzle was shown to increase as the pressure increased. The increase from 13.8 MPa to 69.0 MPa was 2.9 K (70.7%) on the minimum, and 2.6 K (29.9%) on the maximum, temperatures measured.

Good correlation was seen between the upper and lower jet edge frequencies: correlation coefficients were 0.85 and 0.97, respectively.

The jet's lower edge was influenced by temperature at $x/d_n \leq 2$, with correlation coefficients at $x/d_n = 1$ and 2 of 0.80 and 0.87, respectively.

Good correlation existed between the dynamic response of the jetting system and the jet edge fluctuations at $x/d_n = 1$, although this was not found elsewhere.

Strong correlation existed between the jet temperature fluctuations and the dynamic response of the pump, although this decreased as x/d_n increased and the jet temperature increased due to frictional heating at the air-water interface.

Rayleigh-Plesset equation-derived cavitating bubble oscillation frequencies reported elsewhere showed no correlation with the dynamic response of the pump powering this particular water-jet; however, they correlated well with the fluctuations of the jet edges, and showed a similar relationship to the measured temperatures.

This experimental characterisation of a high-pressure water-jet is offered as a baseline case suitable for benchmarking against any of the packages (or models developed on an *ad hoc* basis) used for the numerical analysis and simulation of multi-phase fluid flows.

REFERENCES

[1]   M. Osman, S. Hassan, K. Wan Yusof, Effect of combination factors operating pressure, nozzle diameter and riser height on sprinkler irrigation uniformity. Journal of Advanced Research in Fluid Mechanics and Thermal Science 2 (2014) 1–5.

[2]   E.P. Ying, M.Z. Ngali, N.H. Zakaria, Scaled-down model design of granular fertilizer boom sprayer. Journal of Advanced Research in Applied Mechanics 5 (2015) 1–7.

[3]   S. Sapee, Computational fluid dynamics study on droplet size of kerosene fuel. Journal of Advanced Research in Fluid Mechanics and Thermal Science 16 (2015) 1–14.

[4]   S. Sharafatmandjoor, C.S. Nor Azwadi, Numerical simulation of the dynamics of a droplet in a low-gravitational field. Journal of Advanced Research Design 16 (2016) 15–20.

[5]   Water U.K. Water Industry Specification 4-35-01. Water UK 7 (2000) 13–16.

[6]   W. Tollmien, General instability criterion of laminar velocity distributions. National Advisory Committee Aeronautics Tech. Memo. 792 (1936) Washington DC, USA.
In trans. from; W. Tollmien, Ein allgemeines Kriterium der Instabilität laminarer Geschwindigkeitsverteilungen. Nach. Gesellschaft der Wissenschaften zu Göttingen 1 (1935) 79–114.

[7]   H. Schlichting, Amplitude distribution and energy balance of small disturbances in plate flow. National Advisory Committee Aeronautics Tech. Memo. 1265, (1950) Washington DC, USA.
In trans. from; H. Schlichting, Amplitudenverteilung und Energiebilanz der kleinen Störungen bei der Plattenströmung. Nach. Gesellschaft der Wissenschaften zu Göttingen 1 (1935) 47–78.

[8]   S.A. Campbell, C.A. Fairfield, An overview of the various techniques used in routine cleaning and maintenance of clay, concrete and plastic drains. Construction & Building Materials 163 (2008) 50–60.

[9]   C.A. Fairfield, Cavitation damage to potential sewer and drain pipe material. Wear 317 (2014) 92–103.

[10]   C.A. Fairfield Cavitation erosion resistance of drain and sewer pipe-wall materials: correlations with physico-mechanical, and physico-chemical, properties. Proc. Instn Civ. Engnrs, Construction Materials 168 (2015) 77–91.

[11]   K. Kobayashi, Y. Ito, R. Oba, Unsteady behaviour of cavity boundary directly related to cavity discharge. Proc. 17th Int. Conf. Water Jetting (2004) 317–326.

[12]   S.A. Campbell, An experimental analysis of the behaviour of polymeric and ceramic pipe-wall materials subjected to the action of a cavitating water-jet. PhD thesis, Edinburgh Napier University (2008) Appendix B 415–419.

[13]   C.E. Brennen, S.L. Ceccio, Recent observations on cavitation and cavitation noise. Proc. 3rd Am. Soc. Mech. Engnrs Int. Symp. Cavitation Noise & Erosion Fluid Sys. (1989) 67–78.

[14]   D. Lohse, Bubble puzzles. Physics Today 56 (2003) 36–45.

[15]   C.E. Brennen, Cavitation and Bubble Dynamics. Oxford University Press (1995).